Supplementary Information

Strong Transboundary Electron Transfer of High-entropy Quantum-dots Driving Rapid Hydrogen Evolution Kinetics

Hao Zhao, [ab] Mengyuan Liu, [ab] Qiansen Wang, [ab] YuZe Li, [ab] Yubin Chen, [ac] Yanping Zhu, [c] Zhouying Yue [a], Jun Li [a], Guoliang Wang, [a] Zhiqing Zou [a], Qingqing Cheng*[a] and Hui Yang*[a]

[a] Shanghai Advanced Research Institute, Chinese Academy of Sciences, Shanghai 201210, P. R. China
E-mails: chengqq@sari.ac.cn and yangh@sari.ac.cn

[b] University of Chinese Academy of Sciences, Beijing 100049, P. R. China

[c] Ningbo Cotrun New Energy Science & Technology Co., Ltd., Ningbo 315000, P. R. China

Experimental method

Chemicals and Materials.

$Pt(acac)_2$ (98%), $Ru(acac)_3$ (99%), $Ni(acac)_2$ (95%), $Co(acac)_3$ (99%), $Fe(acac)_3$ (98%), $MoO_2(acac)_2$ (99%) and triethylene glycol (TEG, ≥ 99.5%) were purchased from Adamas. Ethanol (C_2H_6O, ≥ 95%) and cyclohexane (C_6H_{12}, ≥ 99.5%) were purchased from Sinopharm Chemical Reagent Co., Ltd. Other chemicals were bought from Sigma-Aldrich. All reagents were used directly without further purification. Ultrapure water (Millipore Milli-Q grade) with a resistivity of 18.2 MΩ·cm was used in all experiments.

Materials synthesis.

In a typical synthesis of PtRuMoFeCoNi HEA-QDs, 40 mg $Pt(acac)_2$, 40 mg $Ru(acac)_3$, 60 mg $MoO_2(acac)_2$, 60 mg $Fe(acac)_3$, 60 mg $Co(acac)_3$, and 40 mg $Ni(acac)_2$ were dissolved in 50 mL TEG, followed by ultrasonication for 3 h and stirring at 60°C for 30min. The mixture was then rapidly heated in microwave reactor at 230 °C for 80 s. The cooled product was collected by centrifugation and washed six times with a cyclohexane/ethanol (v/v = 1:9) mixture. For the synthesis of PtNi, PtCo, PtRu, PtRuMo, PtCoNi, PtMoFeCoNi (Pt-HEA) and RuMoFeCoNi (Ru-HEA) NPs, all the conditions are similar to that of PtRuMoFeCoNi HEA-QDs except for the difference of acetylacetonate.

Characterizations.

The crystalline structure was determined by Bruker AXS D8 ADVANCE XRD with Cu Kα radiation (λ = 1.5418 Å). The morphologies of HEA-QDs were observed through TEM (JEM-2100F and Tecnai G2 F30 S-Twin, accelerating voltage: 200 kV). Atomic-scale structures and elements distribution were observed via AC-TEM (JEM ARM 200F, accelerating voltage: 200 kV). The metal contents of HEA-QDs were determined by ICP-OES on Agilent ICP-OES 730, with a RF power of 1.0 kW and Ar as the carrier gas. The flow rates of plasma, auxiliary, and nebulizer gases were 15, 1.5, and 0.75 L min^{-1}, respectively. The detection mode was axial, and the calibration type was linear. The dissolution amounts of metal elements during the stability testing were determined by

Perkin Elmer NexION 300D ICP-MS, with a RF power of 1550 W. The flow rates of cooling, auxiliary, and carrier gases were 18, 1.2, and 1.08 L min^{-1}, respectively. The vacuum chamber pressure, deflection voltage, and RF voltage of the mass spectrometer were 6.58×10^{-6} Torr, -10 V, and 200 V, respectively. XPS spectra were recorded on Thermo-scientific ESCALab 250Xi respectively. XAFS spectra (Ru K-edge and Pt L_3-edge) were collected at BL14W1 station in Shanghai Synchrotron Radiation Facility (SSRF) operate at 3.5 GeV with a maximum current of 250 mA. The data were carried out in transmission mode for all samples. Rapid microwave irradiation was conducted using an MCR-3 microwave chemical reactor (900 W) at a stirring speed of 680 rpm.

Electrochemical measurements in a standard three electrode system.

The performance was measured by CHI 760E electrochemical station in a standard three electrode system, using a carbon rod as the counter electrode, a saturated Hg/Hg_2SO_4 electrode as the reference electrode and a glassy carbon electrode (Pine, diameter of 5 mm) as the working electrode. HER measurements were performed in 0.5 M H_2SO_4 solutions at 1600 rpm purged with N_2. The HER polarization curves were collected by the sweep rate of 5 mV s^{-1} without iR compensation. All performance measurements control the precious metal loading to 20 μg cm^{-2}.

All the potentials were calibrated to reversible hydrogen electrode (RHE) according to the **eq 1** below.

$$E(V\ vs.RHE) = E\left(V\ vs.\frac{Hg}{Hg_2\ SO_4}\right) + 0.700\,V + 0.0592 \times pH \quad (1)$$

In the assessment of catalyst stability via chronoamperometry, a uniformly dispersed ink was dropped onto the pre-cut carbon paper substrates (MB30, total carbon paper area of 1×2 cm^2, effectively coated area of 1×1 cm^2), ensuring the noble metal loading of 20 μg cm^{-2} for all samples. The prepared electrode was then used as the working electrode in H-type electrochemical cell. The cell used Nafion 115 membrane as separator, a Pt foil as counter electrode, and a Hg/Hg_2SO_4 electrode as reference electrode. The electrolyte was N_2-saturated 0.5 M H_2SO_4, and all the experiments were conducted at a constant current

density of 50 mA cm^{-2} at 25°C.

The EIS evaluation was performed in a standard three-electrode system under the same conditions as the polarization curve measurements. The EIS measurements were conducted over a frequency range from 1×10^6 Hz to 0.1 Hz with an amplitude of 5 mV. The applied potential corresponded to the potential required for the sample to reach 10 mA cm^{-2}. Based on the typical equivalent circuit models for HER half-cells (insert in **Fig. S25a**), the parameters such as solution resistance (Rs) and charge transfer resistance (Rct) were obtained by fitting the results using nonlinear least squares method.[1]

For the CO stripping measurement, high-purity CO gas was bubbled into 0.5 M H_2SO_4 solution for 30 min, followed by bubbling N_2 for another 30 min to remove the residual CO. Two cycles were recorded to calculate CO stripping peak. The electrochemical accessible surface area of the active sites was obtained using **eq 2** and **eq 3** below.[2]

$$Q_{CO-desorption}(C) = \int i\, dE(mA\,V) \Big/ v\left(\frac{mV}{s}\right) \tag{2}$$

$$ECSA\left(\frac{m^2}{g}\right) = \left[Q_{CO-desorption}(C) \Big/ 420(\mu C/cm^2) M_{noble\ metals}(mg)\right] \times 10^5 \tag{3}$$

The i_0 at the equilibrium potential for Arrhenius and Eyring annalysis was calculated based on the **eq 4**, which is the limiting form of the Butler−Volmer equation at low overpotentials.

$$i = i_0\left(\frac{nF}{RT}\right)\eta \tag{4}$$

For the Arrhenius analysis, rearranging the Arrhenius equation (**eq 5**) and the rate equation of electrochemical reactions (**eq 6**), **eq 7** and its simplified form **eq 8** can be derived. The E_a values of HER can be calculated from the slopes of Arrhenius plot.

$$k = A_f e^{-\frac{E_a}{RT}} \tag{5}$$

Here, k represents the rate constant, A_f is the collision factor or frequency factor and E_a is the activation energy in the reaction.

$$k = \frac{i}{nFAC_{H^+}} \tag{6}$$

Here, i is the current, n is the number of electrons transfer, F is the Faraday constant (96 485 C mol^{-1}), A is the active area of the electrode, and C is the concentration of the reactant (C_{H^+} for HER).

$$logi = \log\left(nFAC_{H^+}A_f\right) - \frac{E_a}{2.303\mathrm{R}} \tag{7}$$

$$logi = \log(K') - \frac{E_a}{2.303\mathrm{RT}} \tag{8}$$

Where K' represents the constant term containing $nFAC_{H^+}A_f$.

For the Eyring analysis, rearranging the Eyring equation (**eq 9**) and the rate equation of electrochemical reactions (**eq 6**), we can obtain the **eq 10** and its simplified form **eq 11**. The Gibbs activation free energy ($\boldsymbol{\Delta G^0}$) values of HER can be determined from the slopes of the Eyring plot.

$$k = \kappa \frac{k_B T}{h} e^{-\frac{\Delta G^0}{RT}} \tag{9}$$

Here, κ represents the symmetry factor, k_B is the boltzmann constant, h is the Planck constant and ΔG^0 is the Gibbs activation free energy in the reaction.

$$log\frac{i}{T} = \log\left(nFAC_{H^+}\kappa\frac{k_B T}{h}\right) - \frac{\Delta G^0}{2.303\mathrm{RT}} \tag{10}$$

$$log\frac{i}{T} = \log(K'') - \frac{\Delta G^0}{2.303\mathrm{RT}} \tag{11}$$

Where K'' represents the constant term containing $nFAC_{H^+}\kappa\frac{k_B T}{h}$.

For the measurement of Faradaic efficiency for H_2 generation, H_2 generated by PEWWE was recorded at 1 A cm^{-2} using drainage method. The theoretical amount of H_2 at 303K was calculated based on Faraday's law and ideal gas law, assuming that 100% of the current was attributed to H_2 production. The Faradaic efficiency of HEA-QDs/C was determined by calculating the ratio of the measured amount of H_2 to the theoretically amount of H_2. Faradaic efficiency was calculated via the **eq12**.

$$Faradaic\ efficiency = \frac{n_{gas}(measured)}{n_{gas}(theoretical)} = \frac{\frac{V}{V_m} \times n \times F}{I \times t} \times 100\% \tag{12}$$

Where V is the volume of collected H_2, V_m is the gas mole volume in 303K, n is the number of electrons transferred to evolve a molecule of the product (in this case, 2), F is Faradaic constant, I is a current, t is the reaction time.

Electrochemical measurements in PEMWE.

Prior to the fabrication of the catalysis coated membrane (CCM), the Nafion 115 membrane was sequentially treated with H_2O_2, 0.5M H_2SO_4, and deionized water at 80 °C for 6h. Commercial IrO_2 was used as an anode electrocatalyst and commercial Pt/C (20 wt. %) or HEA-QDs/C was used as a cathode electrocatalyst. The catalyst ink was prepared by sonicating the mixture of catalyst (Pt/C, IrO_2 or HEA-QDs/C), 5 wt.% Nafion D520 ionomer, deionized water and iso-propanol with a mass ratio of 1: 5: 16: 16. Then a certain quality of anode catalyst ink and cathode catalyst ink were sprayed onto the two sides of the Nafion 115 membrane, respectively, followed by hot-pressing at 135 °C (6 MPa, 4 min). The loading of the anode was 1.5 mg_{IrO2} cm^{-2} and the cathode was 0.1 mg_{PtRu} cm^{-2}

for HEA-QDs or 0.1 mg_{Pt} cm^{-2} for commercial Pt/C. The PEM electrolyzer with the active area of 4 cm^2 was operated at 65 °C and the reactant was deionized water, which was circulated via a peristaltic pump. As shown in **Fig. S30**, the photographs depict present the membrane electrode assembly (MEA), porous transport layer (PTL), bipolar plate, end plate and gasket in PEM cell. PTL is the titanium felt with the thickness of 0.42 mm, and the length×width of 2.2×2.2 cm^2. The bipolar plates used in this work are titanium plates with a thickness of 2 mm, the length×width of 6.0×6.0 cm^2. The effective area of the flow channels on both anode and cathode sides is 2.0×2.0 cm^2. The cathode features parallel flow channels, each with a depth of 0.5 mm and a width of 1 mm. The anode flow channel is a three-channel serpentine design, also with a depth of 0.5 mm and a width of 1 mm. The end plate is made of polytetrafluoroethylene (PTFE). The thickness, length and width are 2, 6, 6 cm, respectively. Gasket is PTFE with the thickness of 0.42 mm and the length×width of 6.0×6.0 cm^2. The ultra-pure water (18.2 MΩ cm) was introduced into the PEWME system through peristaltic pump with the flow rate of 17 ml min^{-1}. The steady state polarization curve of the PEM electrolyzer was collected at the cell voltage of 1.4–2.0 V, and the stability was tested by chronopotentiometry at 1.0 A cm^{-1} for 1 000 h.

For the PEMWE configuration, the EIS evaluation was also performed in a three-electrode system. The wet H_2-saturated cathode served as both the reference electrode and counter electrode while the anode acted as working electrode. EIS measurements were performed over a frequency range from 1×10^6 Hz to 0.1 Hz with an amplitude of 10 mV. The potentials applied to the working electrode were 1.4V, 1.5V, and 1.6V. Based on the typical equivalent circuit models for PEMWE (**Fig. S40a**), the parameters were obtained by fitting the results using nonlinear least squares method.[3]

The calculation of hydrogen cost in PEMWE was based on **eq 13** to **eq 16** below.

$$\text{Mass of } H_2 = \frac{j(\text{current density})\times A(\text{electrolyzer area})\times t(\text{working time})\times \text{molar mass } H_2}{2\times F}$$

$$= \frac{1.0\ \text{A cm}^{-2}\times 4\ \text{cm}^2\times 1000\ \text{hours}\times 3600\ \frac{\text{s}}{\text{hours}}\times 2\ \text{g mol}^{-1}}{2\times 96485\ \text{c mol}^{-1}} = 149.24\ \text{g} \quad (13)$$

$$\text{Volume of } H_2 = \frac{\text{m}}{\rho} = \frac{149.24\ \text{g}}{0.09\ \text{g L}^{-1}} = 1658.28\ \text{L} \quad (14)$$

$$\text{Energy consumption} = \frac{1.65\ \text{V}\times 4\ \text{A}\times 1000\ \text{hours}}{0.1492\ \text{kg}} = \frac{44.236\ \text{kWh}}{\text{kg } H_2} = \frac{3.98\ \text{kWh}}{\text{m}^3\ H_2} \quad (15)$$

$$\text{Cost per kilogram of } H_2 = \text{energy consumption} \times \text{electricity bill}$$

$$= \frac{44.236\ \text{kWh}}{\text{kg } H_2} \times \frac{\text{US\$ } 0.02}{\text{kWh}} = \frac{\text{US\$ } 0.88}{\text{kg } H_2} \quad (16)$$

Computational methods.

All DFT calculations were carried out using the Vienna ab initio simulation package (VASP).[4] The Perdew-Burke-Ernzerhof (PBE) functional of generalized gradient approximation was used to treat the exchange-correlation interactions.[5] The plane wave basis set with a kinetic energy cutoff of 400 eV and the energy convergence criterion of 10^{-4} eV was used for structure relaxation. Projector augmented wave (PAW) pseudopotentials were used to describe the ionic cores. A vacuum region more than 12 Å along the c-axis was set to prevent the interaction between two adjacent periodic images. All surface calculations used a (2×2×1) Monkhorst-Pack k-point sampling. H_2O and H_2 were calculated in boxes of 15 Å×15 Å×15 Å, with the gamma point only. The free energy diagrams for HER were calculated with reference to the computational hydrogen electrode (CHE).[6] The CHE model uses one half of the chemical potential of gaseous hydrogen ($\mu(H_2)$) as the chemical potential of the proton–electron pair ($\mu(H^+/e^-)$). The free energy of each species can be obtained from the **eq 17**:

$$\Delta G = \Delta E_{DFT} + \Delta ZPE - T\Delta S \quad (17)$$

Where ΔE_{DFT} is the electronic energy, T was set as 298.15 K. ZPE and TΔS are the change in the zeropoint energy and entropy at room temperature (T=298.15 K), which are obtained after frequency calculations.

As depicted in **eq 18**, the electrode potential is determined by referring the system's work function (Φ) to the experimental work function of the standard hydrogen electrode (SHE)[7], and Φ_{SHE} has been determined experimentally to be ~4.4 eV.[8, 9]

$$U_{SHE} = (\Phi - \Phi_{SHE})/e \quad (18)$$

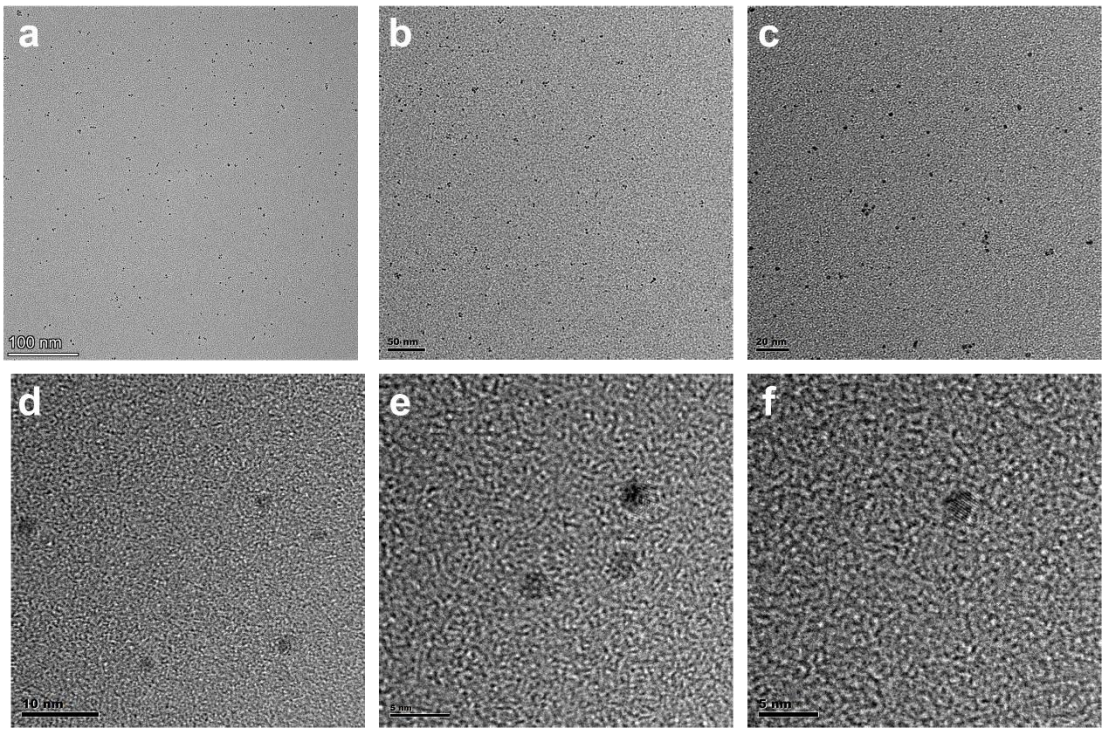

Supplementary Figure 1. (a-f) TEM images of HEA-QDs at different scales.

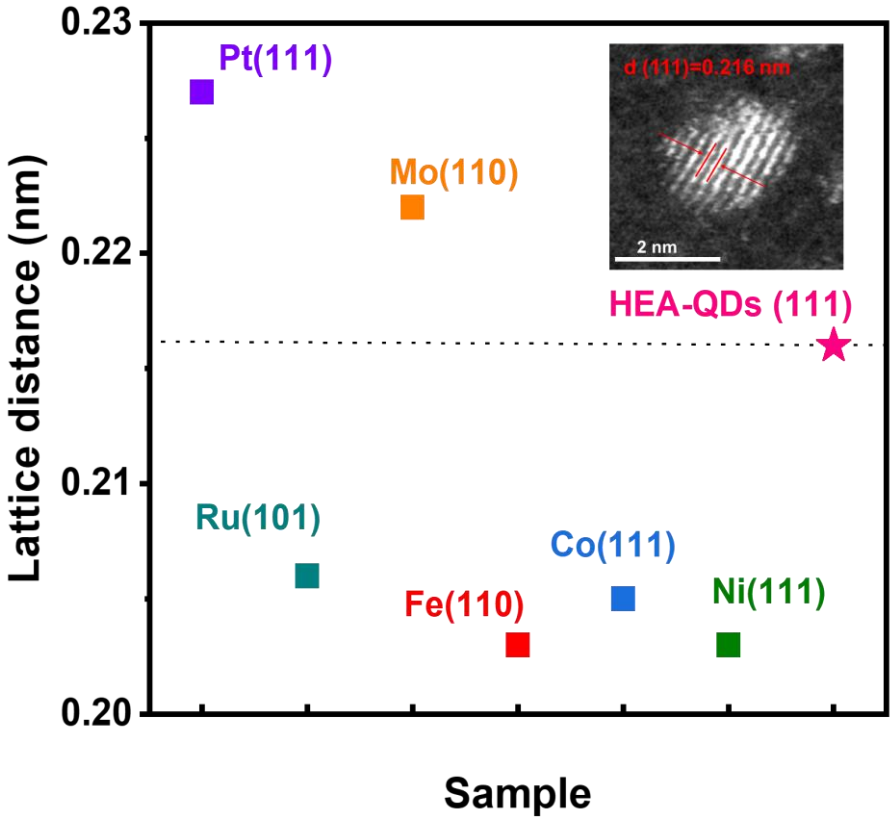

Supplementary Figure 2. The lattice distances of HEA-QDs (111) and other pure metals including Pt (111), Mo (110), Ru (101), Fe (110), Co (111) and Ni (111). Inset image is the HAADF-STEM image of HEA-QDs.

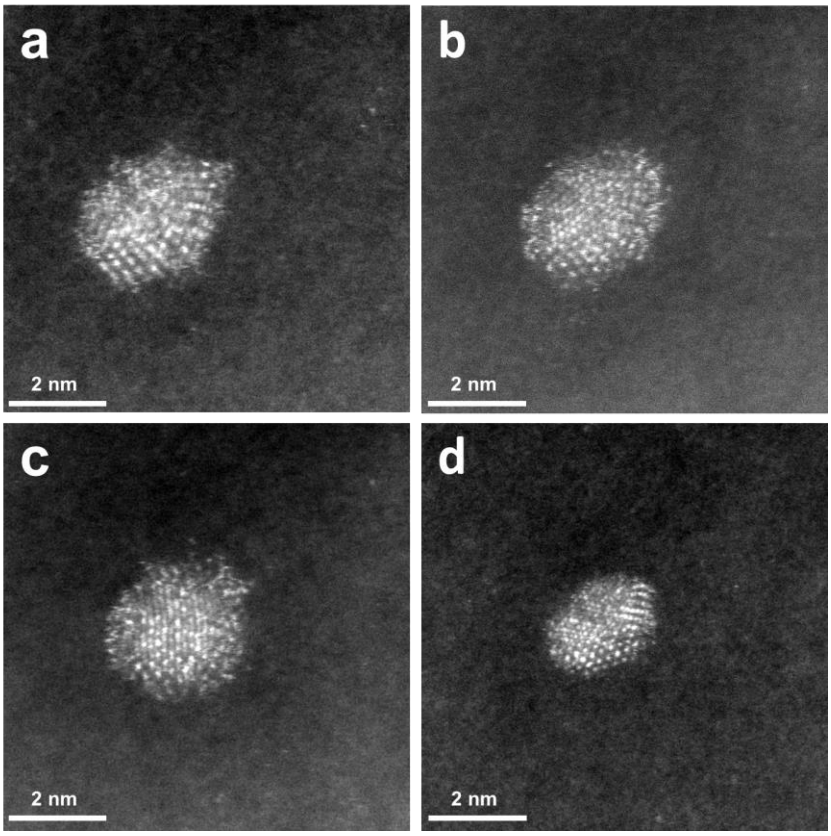

Supplementary Figure 3. (a-d) HADDF-STEM images of HEA-QDs.

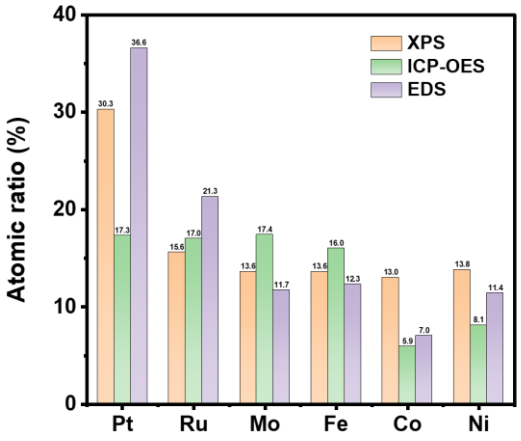

Supplementary Figure 4. The atomic ratios of different metals in HEA-QDs obtained from XPS, EDS and ICP-OES.

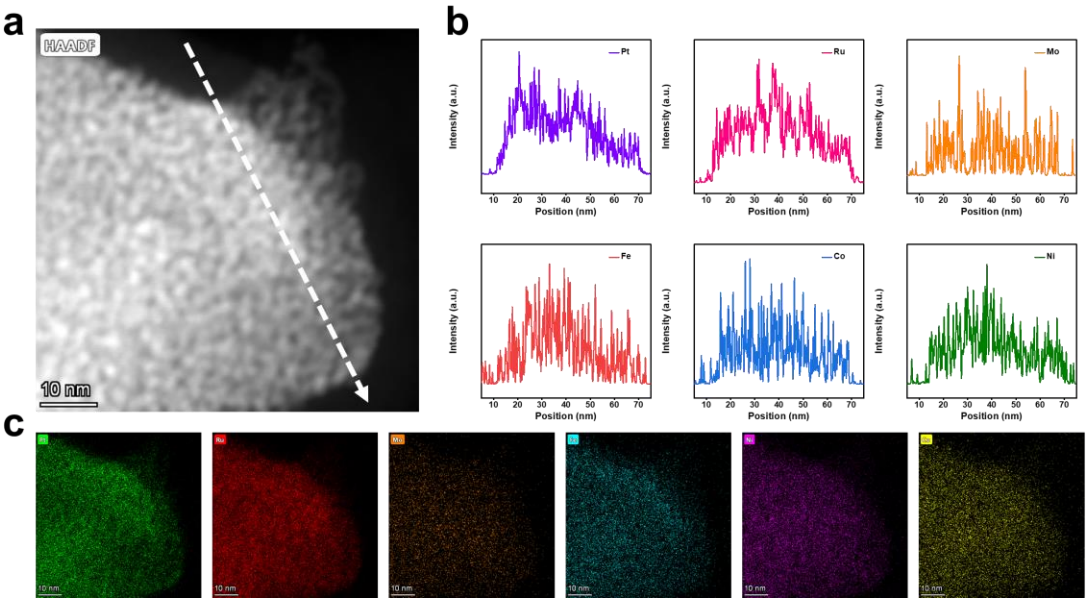

Supplementary Figure 5. (a) HAADF-STEM image of HEA-QDs and corresponding (b) line scan profile and (c) EDS elemental mappings.

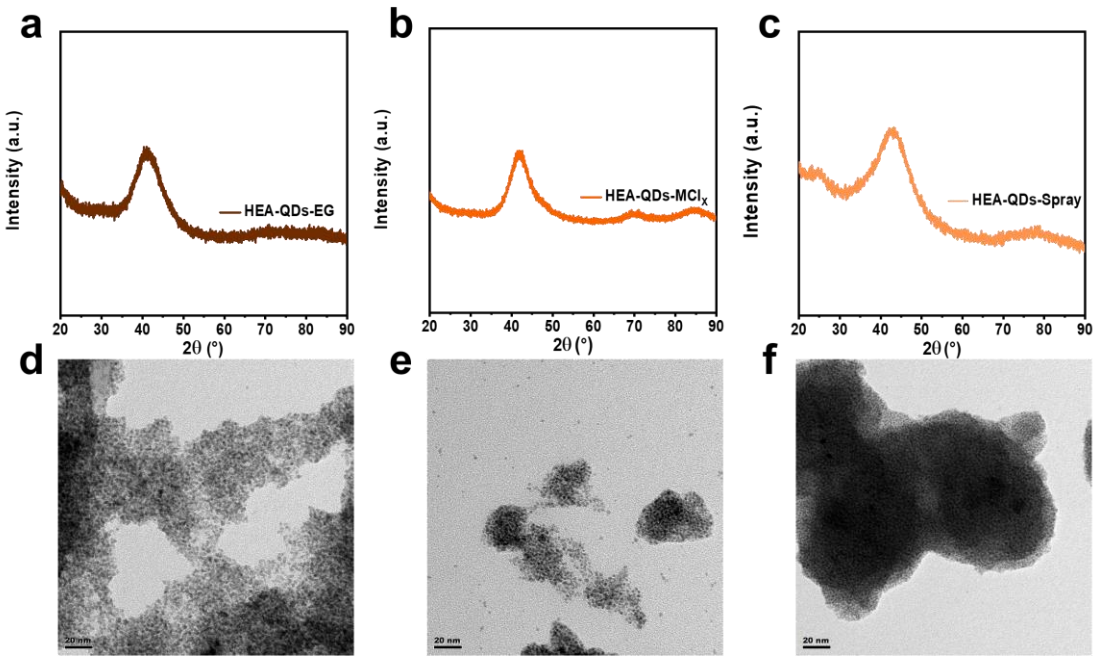

Supplementary Figure 6. (a-c) XRD patterns and (d-f) TEM images of the products with the same reaction conditions as those of HEA-QDs except (a, d) using EG instead of TEG; (b, e) using chlorine salt instead of acetylacetone salt; (c, f) using spray reduction instead of microwave reduction.

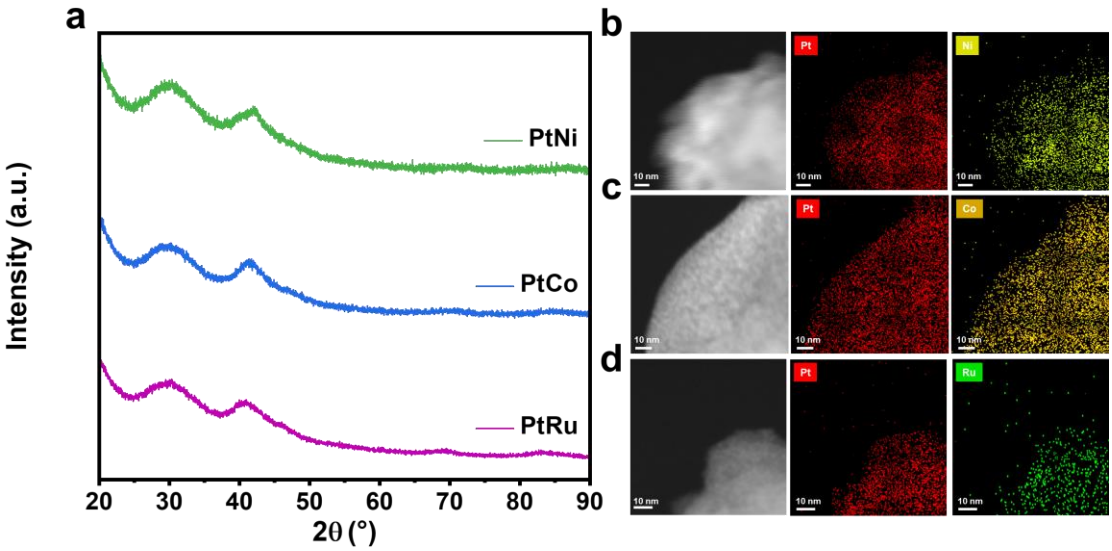

Supplementary Figure 7. (a) XRD pattern of PtNi, PtCo and PtRu. (b, c, d) HADDF-STEM images and corresponding EDS elemental mappings of PtNi, PtCo and PtRu, respectively.

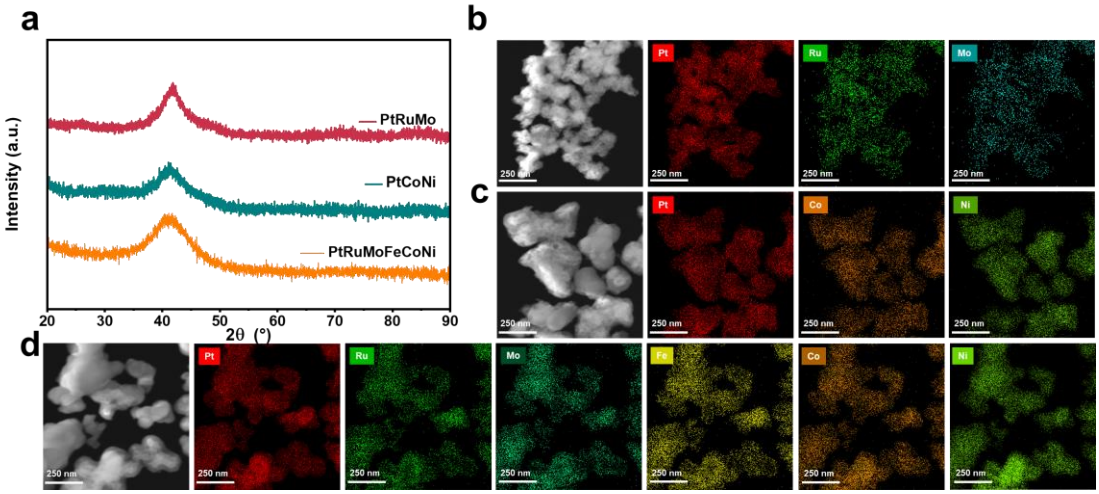

Supplementary Figure 8. (a) XRD pattern of PtRuMo, PtCoNi and PtRuMoFeCoNi. (b, c, d) HADDF-STEM images and corresponding EDS elemental mappings of PtRuMo, PtCoNi and PtRuMoFeCoNi, respectively.

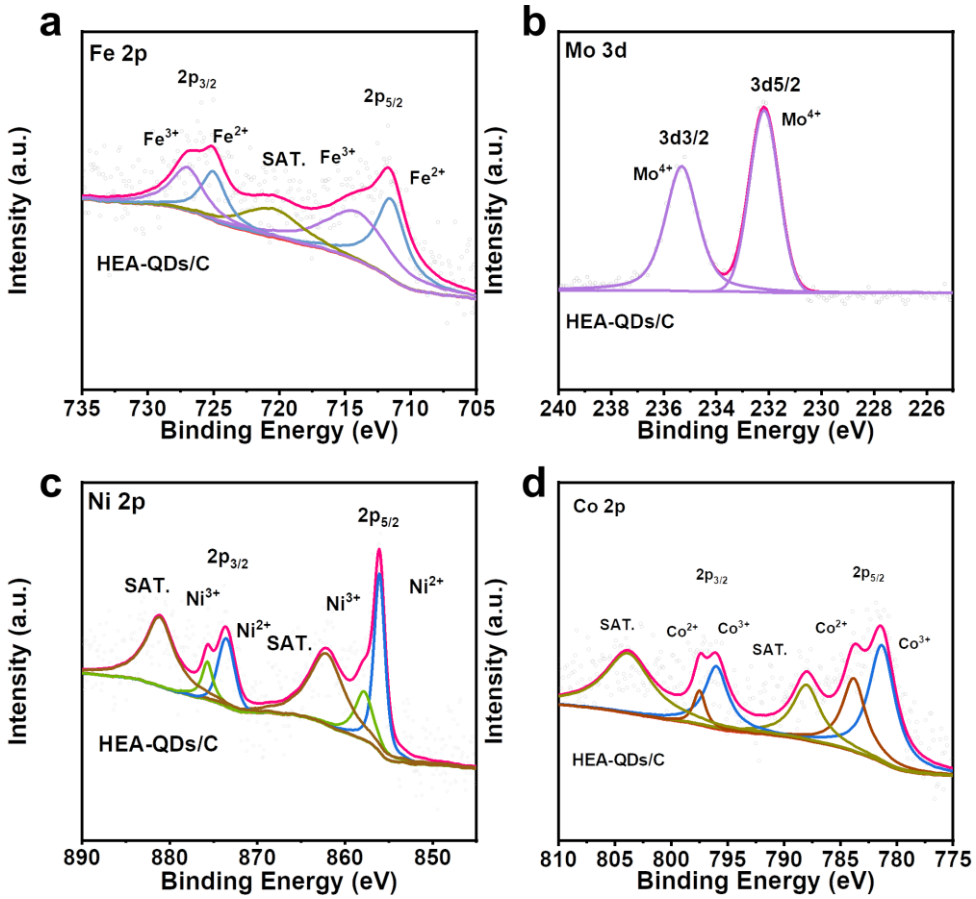

Supplementary Figure 9. XPS spectra of (a) Fe 2p, (b) Mo 3d, (c) Ni 2p and (d) Co 2p in HEA-QDs.

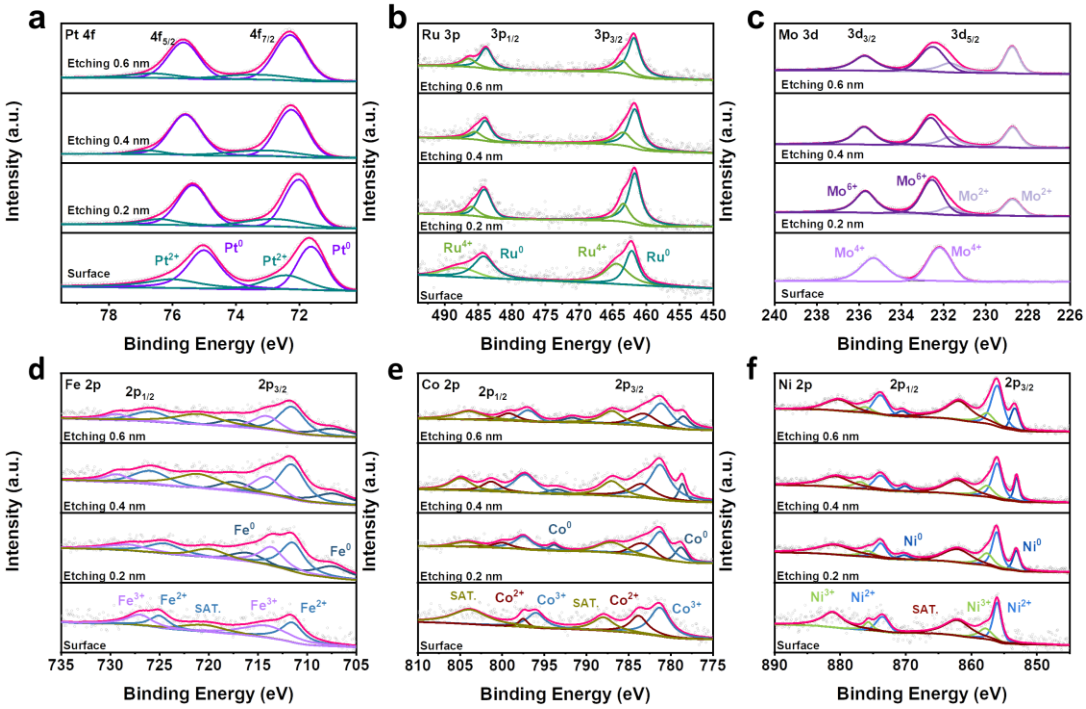

Supplementary Figure 10. XPS spectra at different depths of (a) Pt 4f, (b) Ru 3p, (c) Mo 3d, (d) Fe 2p, (e) Co 2p and (f) Ni 2p in HEA-QDs.

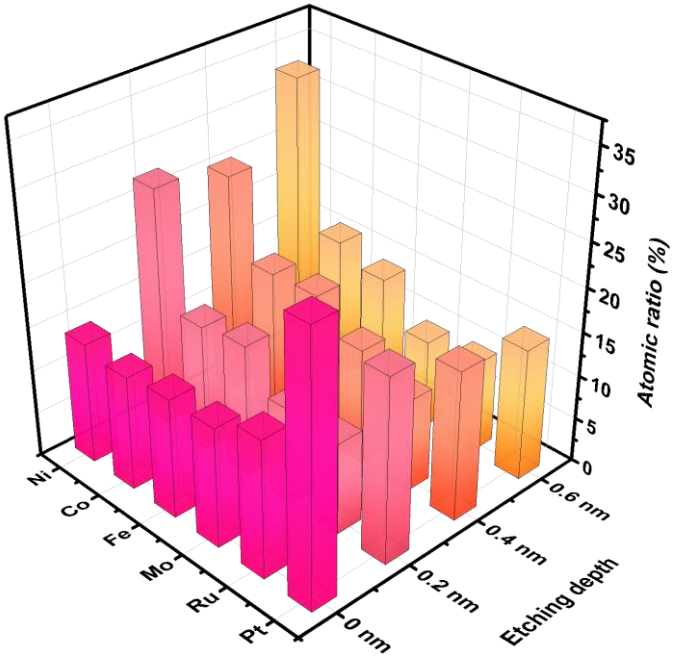

Supplementary Figure 11. The atomic radio of Pt, Ru, Mo, Fe, Co and Ni at different depths in HEA-QDs.

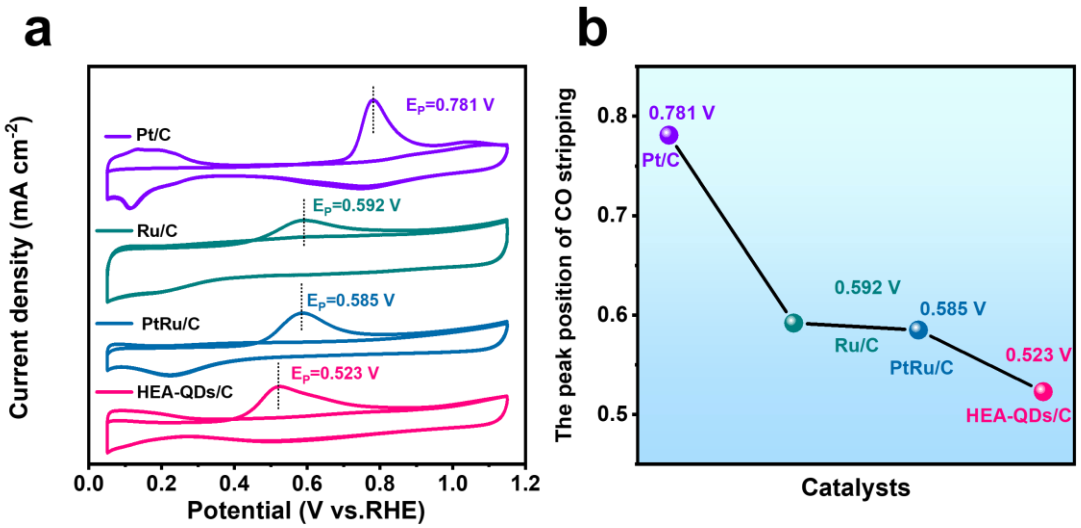

Supplementary Figure 12. (a) The CO stripping curves of HEA-QDs/C, Pt/C, Ru/C and PtRu/C. (b) The peak positions of CO stripping for HEA-QDs/C, Pt/C, Ru/C and PtRu/C.

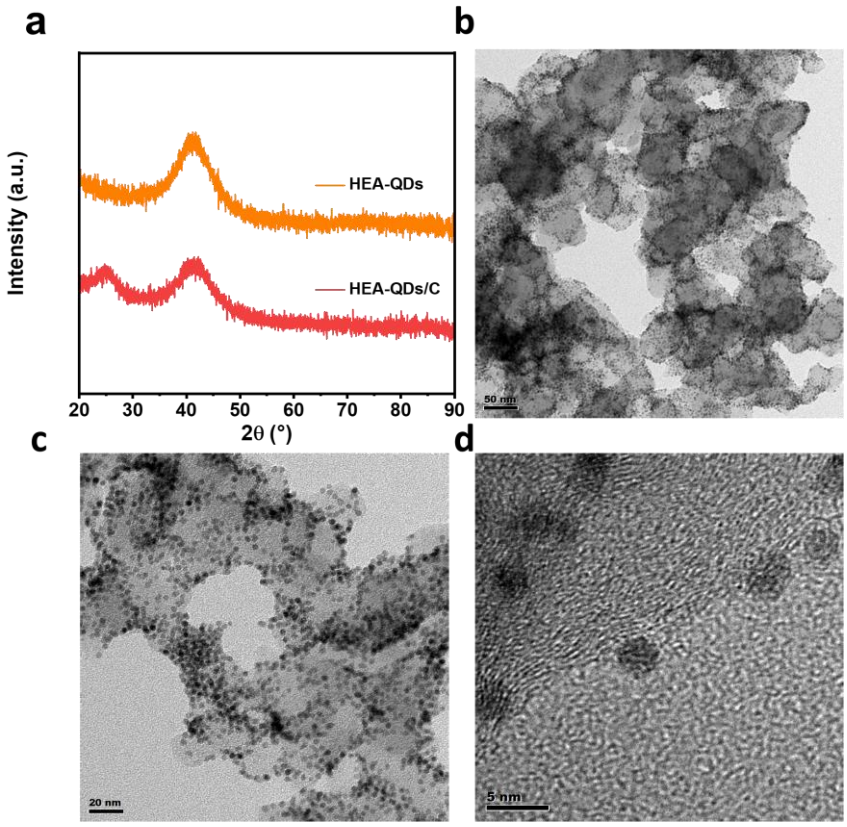

Supplementary Figure 13. (a) XRD pattern of HEA-QDs and HEA-QDs/C. (b-d) TEM images of HEA-QDs/C at different scales.

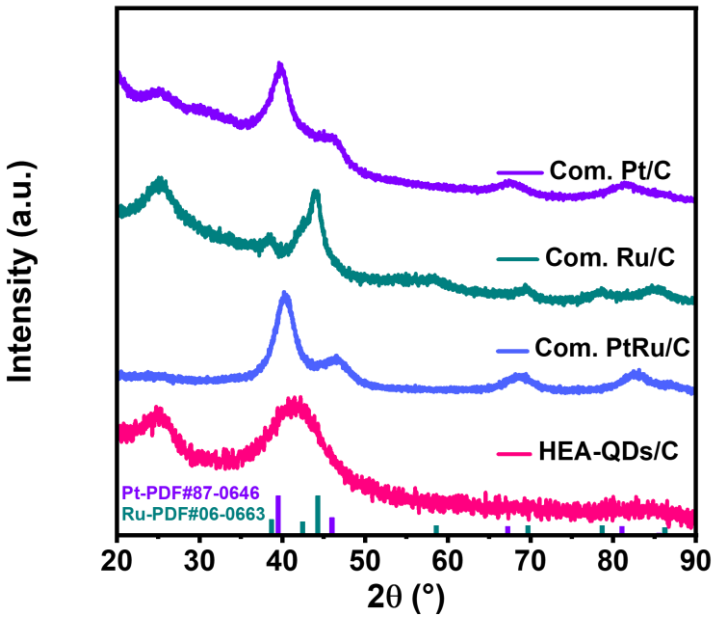

Supplementary Figure 14. XRD pattern of commercial Pt/C, Ru/C, PtRu/C and HEA-QDs/C.

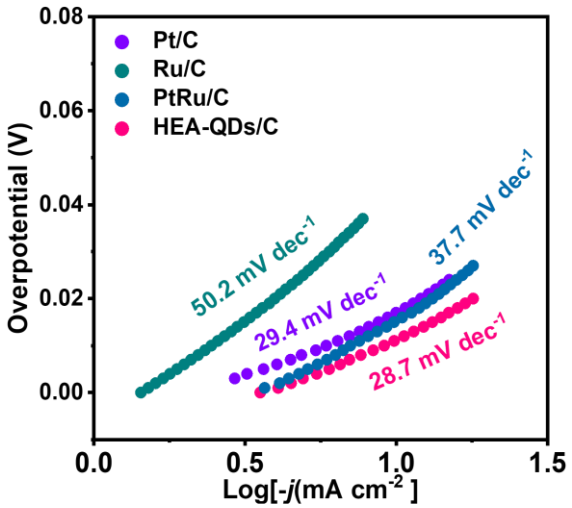

Supplementary Figure 15. Tafel plots of commercial Pt/C, commercial Ru/C and HEA-QDs/C.

Table S1. Comparison between HEA-QDs/C and other reported catalysts for acidic HER.

Catalysts	Electrolyte	η_{10} (mV)	Tafel slope (mv dec^{-1})	Ref.
HEA-QDs/C	**0.5 M H_2SO_4**	**11**	**28.7**	**This work**
$PtRu/CC_{1500}$	0.5 M H_2SO_4	8	25	10
Ru@GnP	0.5 M H_2SO_4	23	30	11
Pt-AC/DG	0.5 M H_2SO_4	21	27.5	12
$Ru@C_2N$	0.5 M H_2SO_4	22	30	13
Pt/Ni-PCNFs-50	0.5 M H_2SO_4	20	30.9	14
Pt_1Ru_1/NMHCS-A	0.5 M H_2SO_4	22	38	15
Ru@NC	0.5 M H_2SO_4	62	40	16
$Pt_{0.47}$-Ru/Acet	0.5 M H_2SO_4	28	33.3	17
Pt-TiO_2-N-rGO	0.5 M H_2SO_4	40	32	18
HP-Ru/C	0.5 M H_2SO_4	38	39	19
Ni@Ni_2P–Ru	0.5 M H_2SO_4	51	35	20
Ru/HMCs-500	0.5 M H_2SO_4	48	40.4	21
Ru/D-NPC	0.5 M H_2SO_4	68	41.7	22
$MoS_2/CoSe_2$	0.5 M H_2SO_4	68	36	23
A-Ni–C	0.5 M H_2SO_4	34	31	24
$WO_{2.9}$	0.5 M H_2SO_4	70	50	25
NiRuPt/Activated XC-72	0.5 M H_2SO_4	22.4	23.9	26
m-Pt@MoS_2	0.5 M H_2SO_4	47	32	27
Ru−Mo_2C/C	0.5 M H_2SO_4	18	32	28
Ru_2@MoS_2-85%/CFP	0.5 M H_2SO_4	54	49	29
RuSA@NiFe PPc	0.5 M H_2SO_4	40	31	30
Ru-VO_2	0.5 M H_2SO_4	46	27.7	31

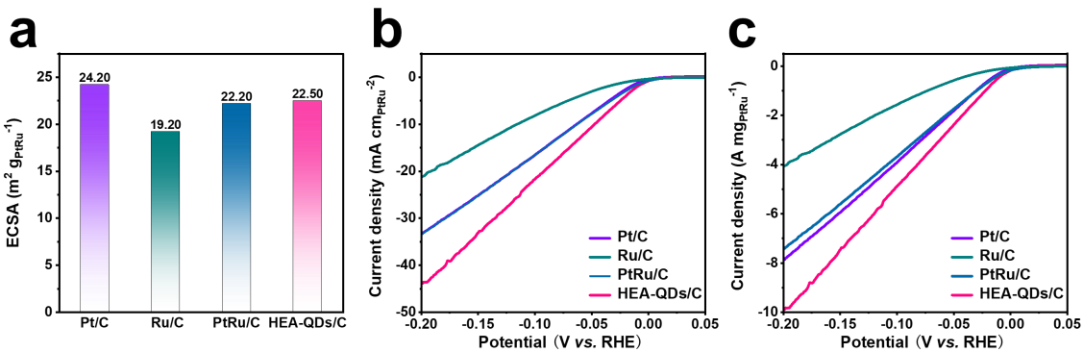

Supplementary Figure 16. (a) Calculated ECSA based the results of CO stripping, (b) calculated SA and (c) MA of Pt/C, Ru/C, PtRu/C and HEA-QDs/C.

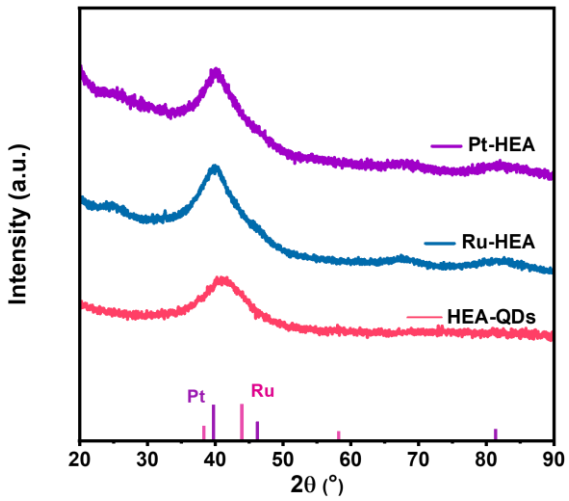

Supplementary Figure 17. The XRD patterns of Pt-HEA, Ru-HEA and HEA-QDs.

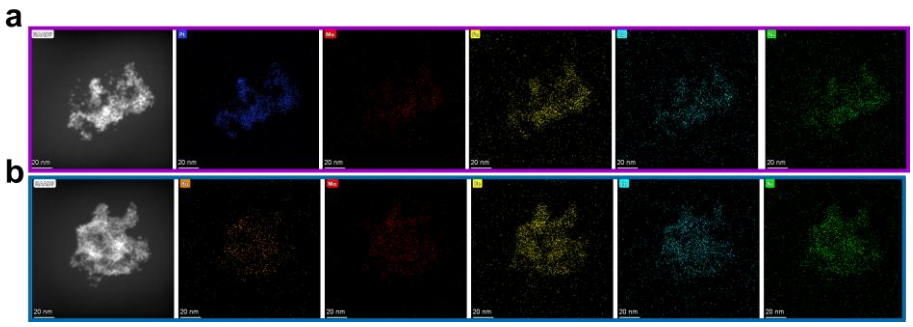

Supplementary Figure 18. The TEM images and corresponding EDS mappings of (a) Pt-HEA and (b) Ru-HEA.

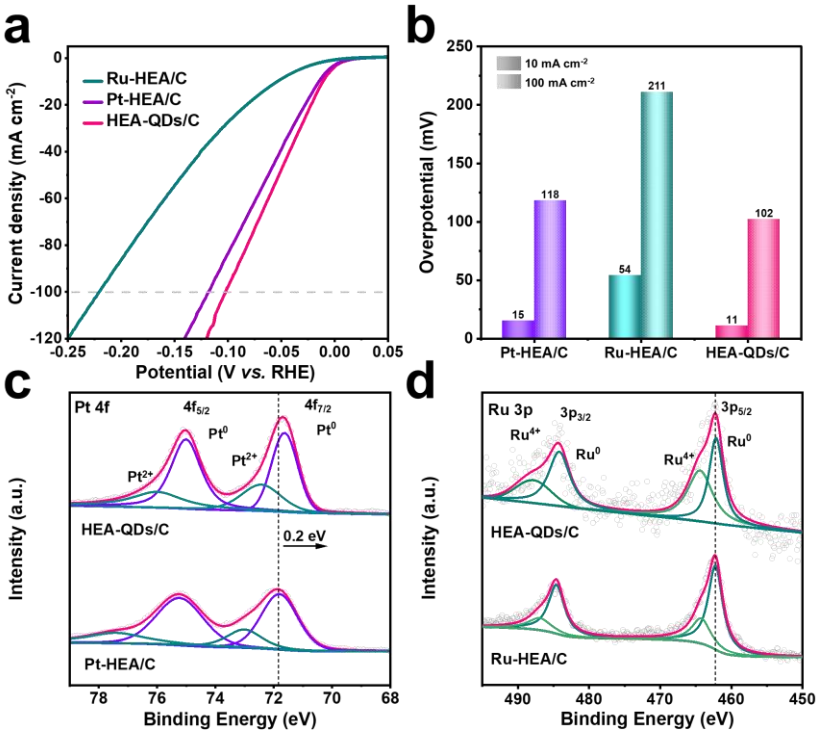

Supplementary Figure 19. (a) The polarization curves, (b) overpotential at 10/100 mA cm^{-2}, XPS spectra of (c) Pt and (d) Ru of Pt-HEA/C, Ru-HEA/C and HEA-QDs/C.

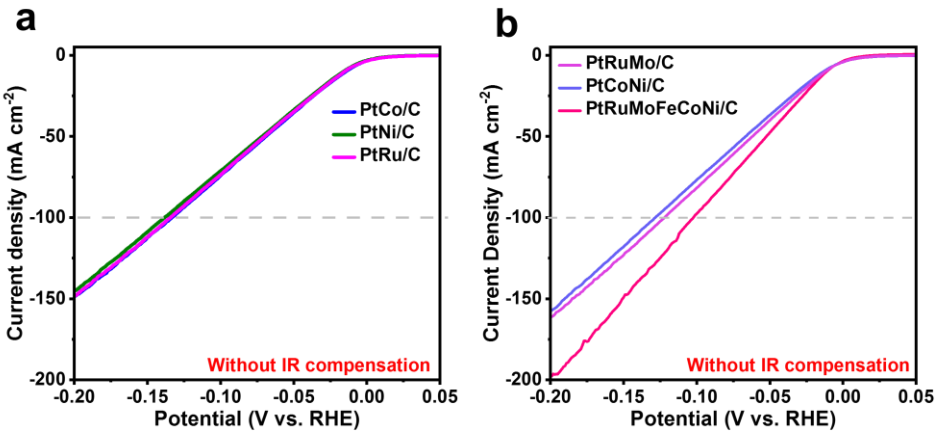

Supplementary Figure 20. (a) Polarization curves of PtCo/C, PtNi/C and PtRu/C. (b) Polarization curves of PtCoNi/C, PtRuMo/C and PtRuMoFeCoNi/C.

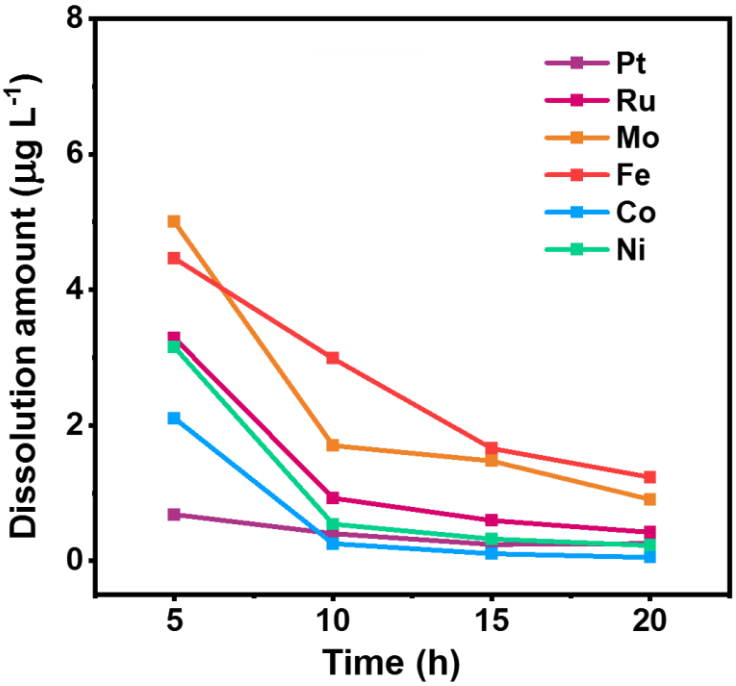

Supplementary Figure 21. Time-dependent metal cations' concentration in electrolyte.

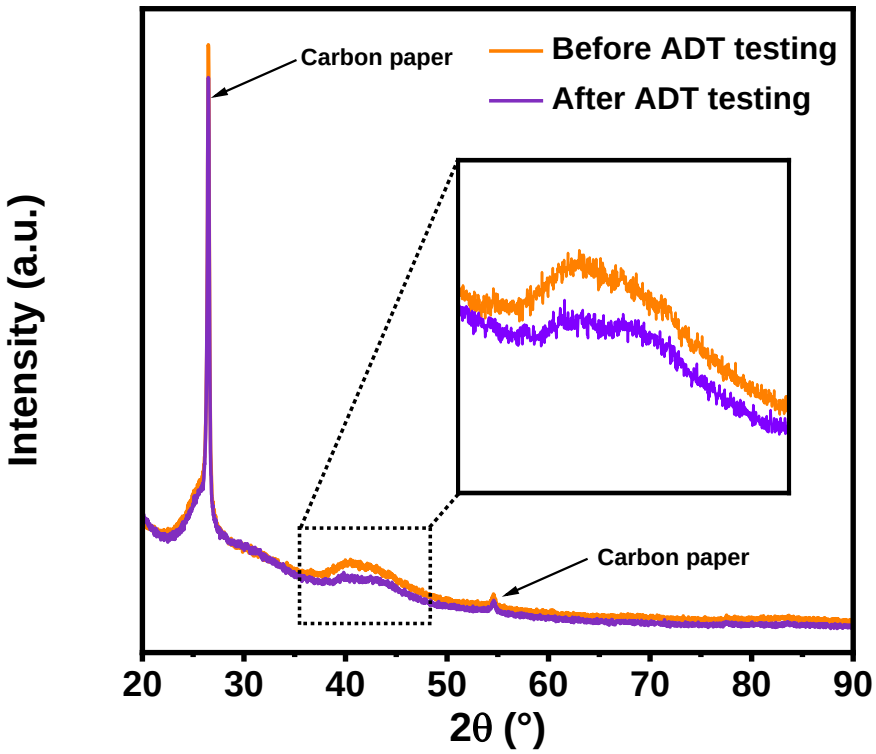

Supplementary Figure 22. XRD pattern of HEA-QDs before and after ADT test.

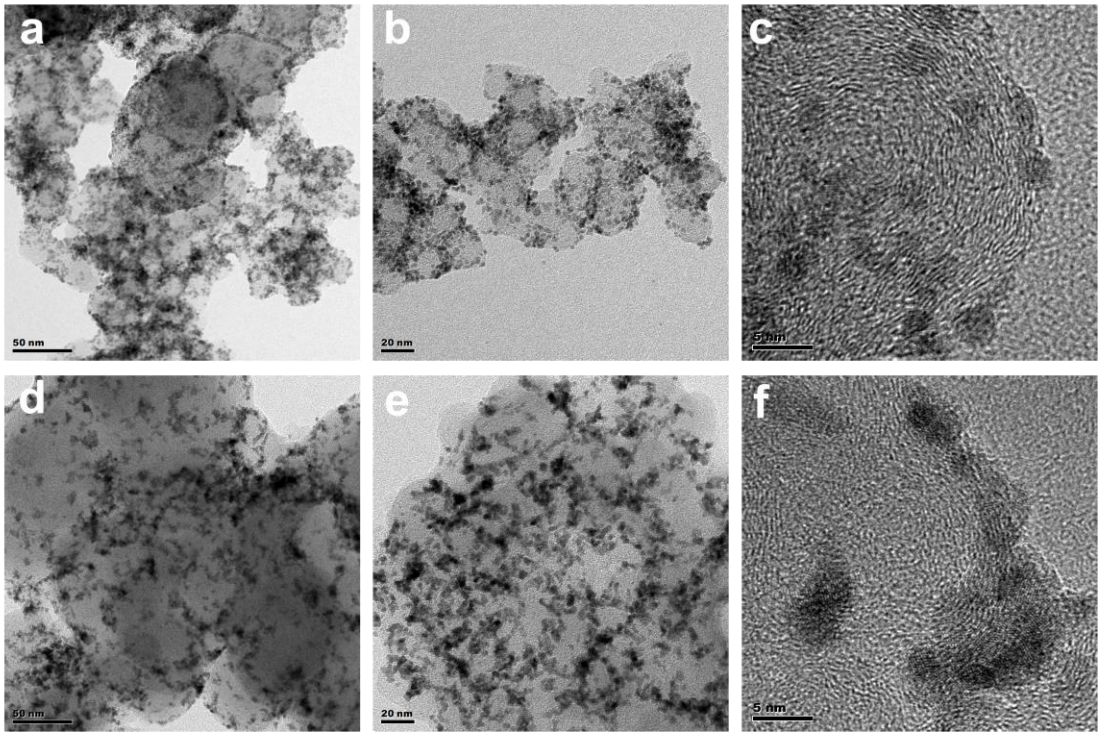

Supplementary Figure 23. TEM images of HEA-QDs before (a, b, c) and after (d, e, f) ADT test.

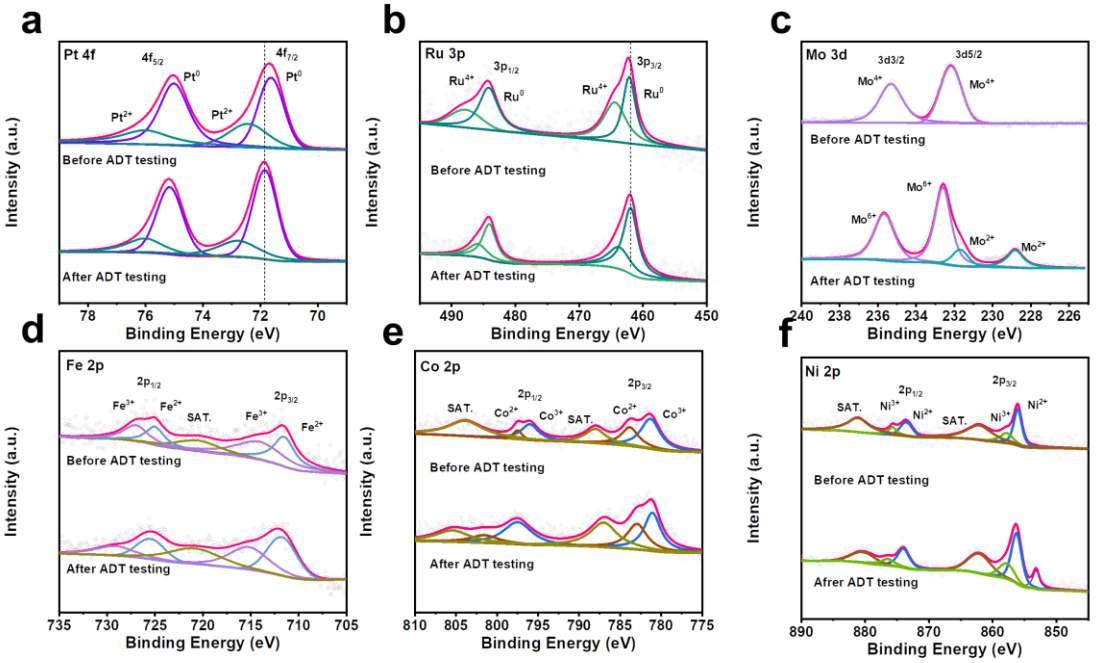

Supplementary Figure 24. XPS spectra of HEA-QDs before (a, b, c) and after (d, e, f) ADT test.

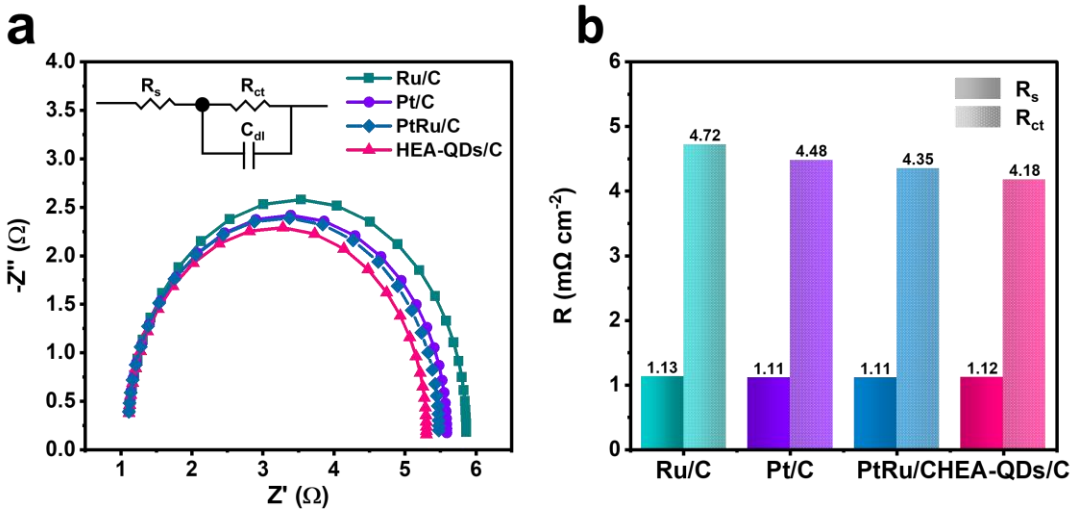

Supplementary Figure 25. (a) Electrochemical Impedance Spectroscopy (EIS) Nyquist plots of commercial Pt/C, Ru/C, PtRu/C and HEA-QDs/C at the current density of 10 mA/cm^2. (b) The calculated R_s and R_{ct} according to the Nyquist plots.

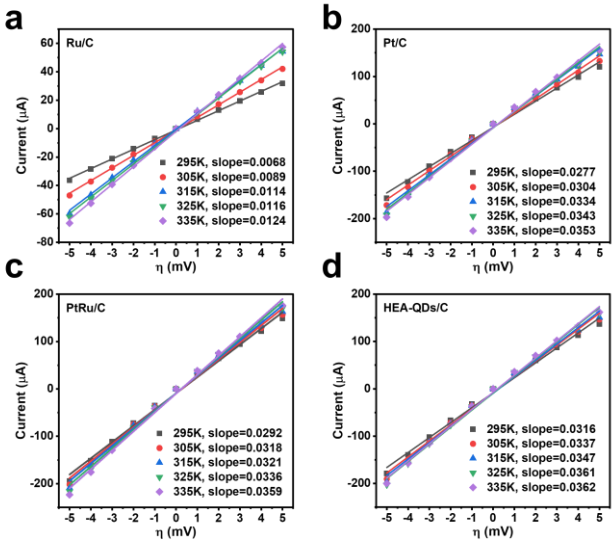

Supplementary Figure 26. Polarization curves of (a) Ru/C, (b) Pt/C, (c) PtRu/C and (d) HEA-QDs/C in the micro-polarization region in hydrogen-saturated 0.05 M H_2SO_4 at a temperature range of 295–335 K.

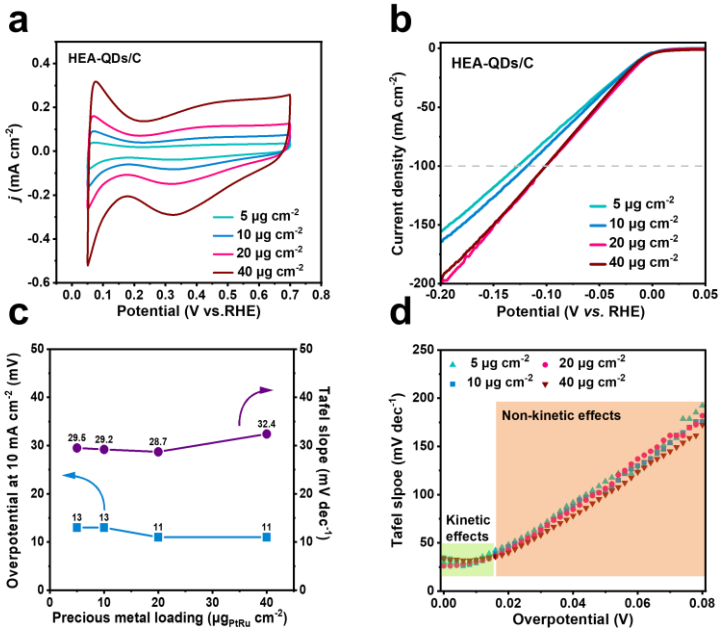

Supplementary Figure 27. (a) CV curves, (b) polarization curves, (c) Tafel slope values and the overpotential at 10 mA cm^{-2}, and (d) Tafel slope values vs. the potential (Tafel slope obtained over 10 mV intervals) of HEA-QDs/C with different loadings.

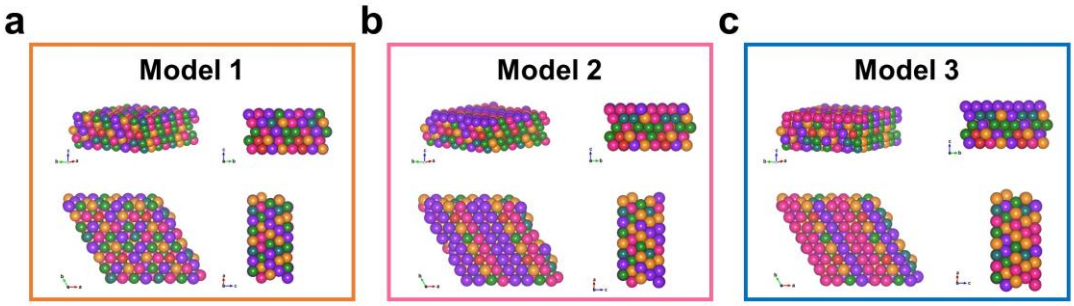

Supplementary Figure 28. The various model structures of HEA-QDs with different perspectives for (a) Model 1, (b) Model 2 and (c) Model 3.

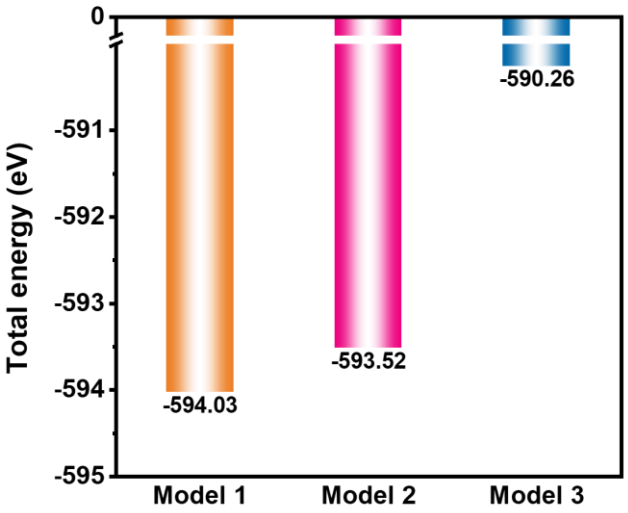

Supplementary Figure 29. The calculated total energy various model structures.

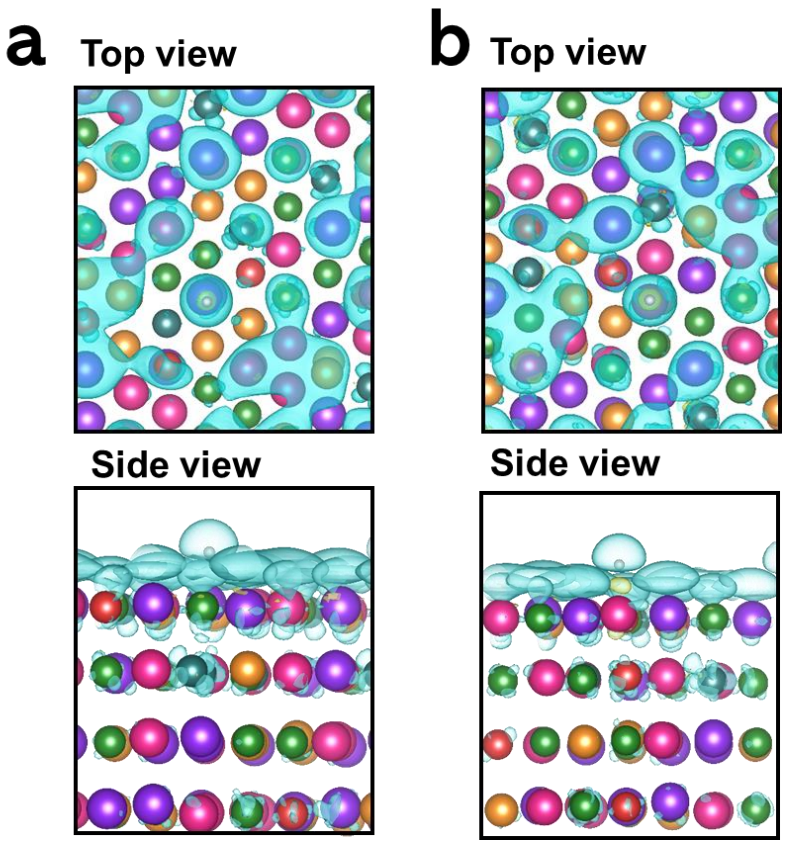

Supplementary Figure 30. (a) Charge difference density plots of HEA-QDs with *H adsorbed on the top of the Pt atom when 0.7371e^- is added (difference between potentials of -0.1 V vs SHE and 0 V vs SHE). (b) Charge difference density plots of HEA-QDs with *H adsorbed on the top of the Ru atom when 1.07e^- is added (difference between potentials of -0.1 V vs SHE and 0 V vs SHE). The electron accumulation and depletion are represented with cyan and yellow contours, with iso-surfaces being 0.0003 e/Å^3.

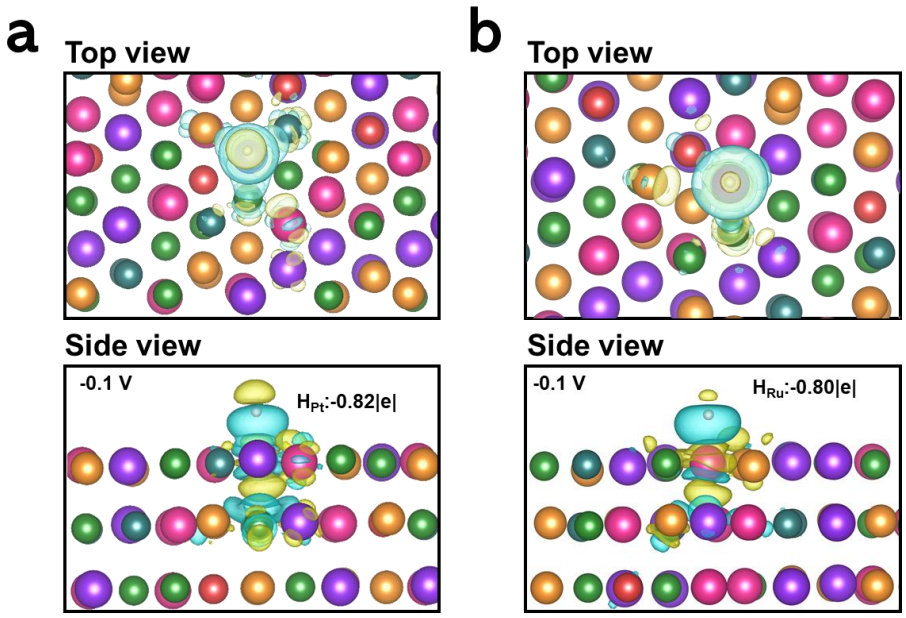

Supplementary Figure 31. Charge difference density plots of adsorption of *H onto the top of the (a) Pt atom and (b) Ru atom in the surface of HEA-QDs under a potential of -0.1 V vs SHE. The electron accumulation and depletion are represented with cyan and yellow contours, with iso-surfaces being 0.002 e/Å^3.

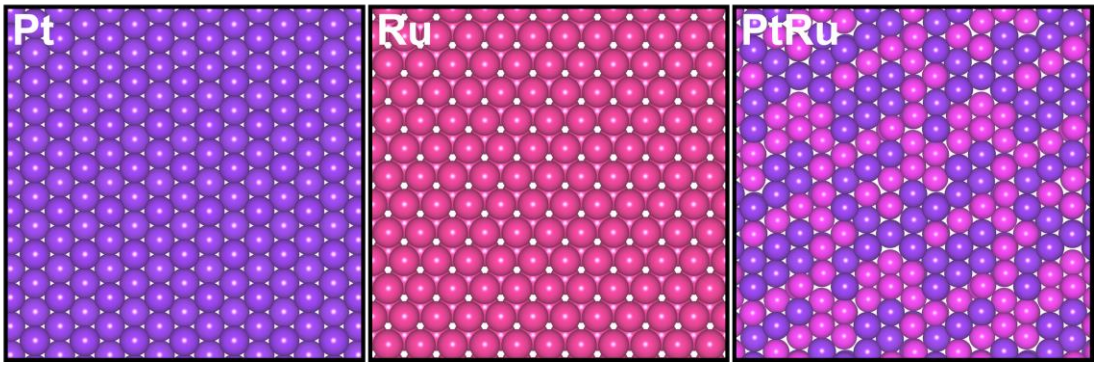

Supplementary Figure 32. The atomic structure mode of pure Pt, pure Ru and PtRu.

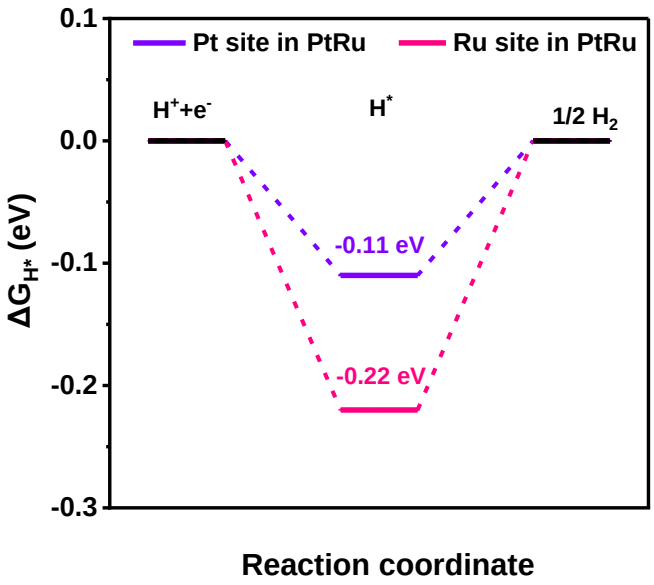

Supplementary Figure 33. Calculated hydrogen-adsorption free energy (ΔG_{H^*}) profiles for Pt and Ru sites on PtRu.

Table S2. The Decomposition of the Tafel activation barriers of $H^*+H^*\rightarrow H_2$ on HEA-QDs (111), Pt (111) and Ru (001).

$H^*+H^*\rightarrow H_2$	E_{H^*1} (eV)	E_{H^*2} (eV)	E_g (eV)	E_e (eV)	E_{TS} (eV)
Pt site on HEA-QDs	0.60	0.62	1.22	-0.42	0.80
Ru site on HEA-QDs	0.24	0.29	0.53	-0.11	0.42
Pt site on Pt (111)	0.28	0.53	0.81	0.03	0.84
Ru site on Ru (001)	0.35	0.45	0.79	-0.26	0.53

Where E_g and E_e represent the contribution of geometrical effects and local electronic effect to the activation energy, respectively.

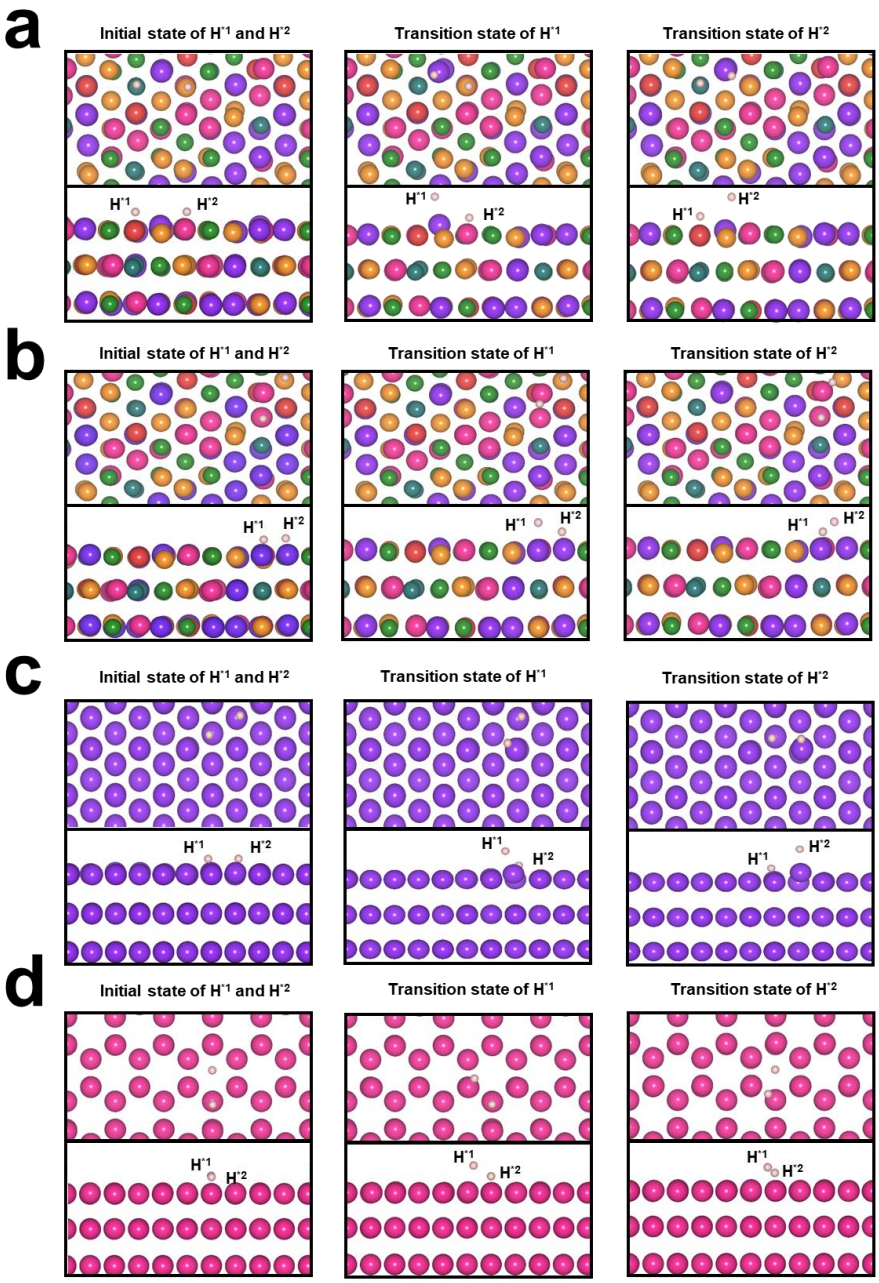

Supplementary Figure 34. Schematic diagrams of H^{*1} and H^{*2} in initial states and transition states of (a) Pt sites on HEA-QDs, (b) Ru sites on HEA-QDs, (c) Pt sites on Pt (111) and (d) Ru sites on Ru (001).

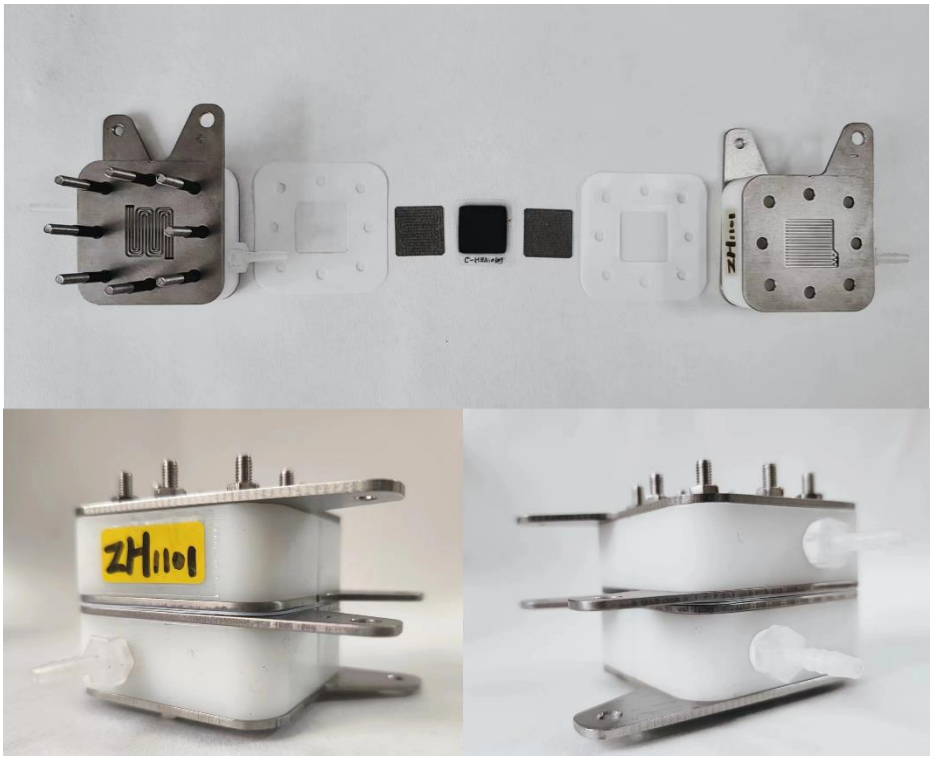

Supplementary Figure 35. Photographs of the PEM electrolyzer at different perspectives.

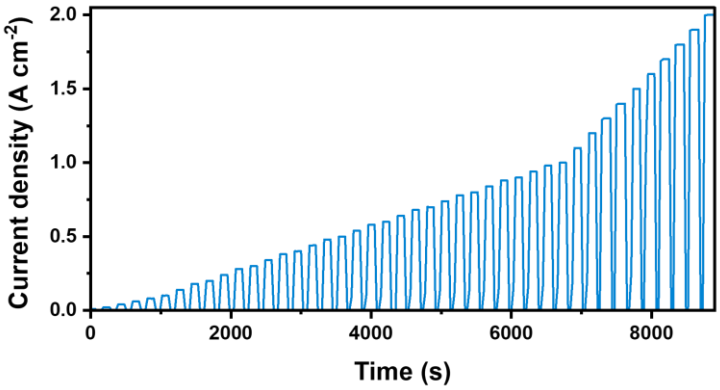

Supplementary Figure 36. The applied current density as a function of time in the testing of steady-state polarization curve for PEMWEs.

The PEMWE polarization curves were evaluated under steady-state conditions. As shown in **Fig. S36**, the cell was stabilized for 120 seconds at each current density from 0.01 to 2.0 A cm^{-2}, and the corresponding voltage was recorded. Between each current density measurement, the cell was allowed to rest for 30 seconds to eliminate any transient effects. The voltage at the end of each stabilization period was recorded as the steady-state voltage for that current density, and these values were used to plot the polarization curves.

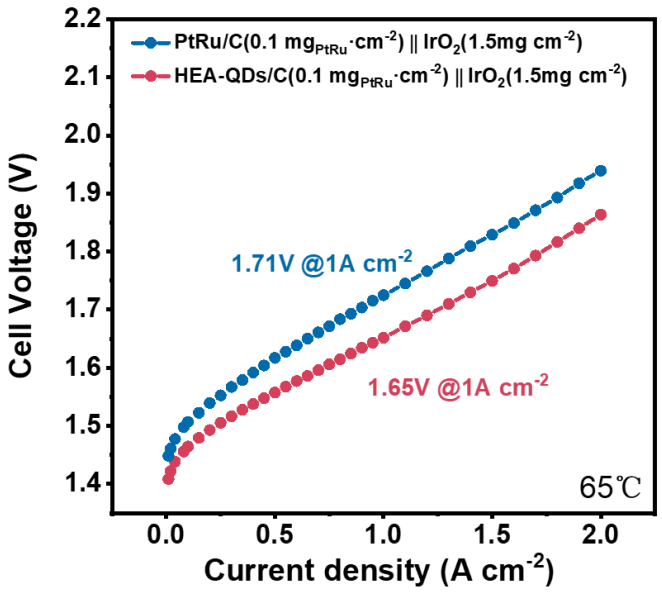

Supplementary Figure 37. Polarization curves of PEMWEs at 65°C with the cathode catalysts of PtRu/C and HEA-QDs/C.

Table S3. The comparison of PEMWE performance in this work with other recent works.

Cathode catalyst	Cathode loading (mg_{PGM} cm^{-2})	Anode catalyst	Anode loading (mg_{PGM} cm^{-2})	PEM	Temperature (℃)	Performance	Ref.
HEA-QDs/C	0.1	IrO_2	1.5	N115	65	1.65 V@1 A cm^{-2}	This work
20% Pt/C	0.1	IrO_2	1.5	N115	65	1.71 V@1 A cm^{-2}	This work
20% Pt/C	0.3	IrO_2	1.5	N115	65	1.64 V@1 A cm^{-2}	This work
Pt-NCS-2	0.1	IrO_2	0.1	N117	60	2.1 V@0.435 A cm^{-2}	[32]
PtNW	0.1	$Ir_{0.7}Ru_{0.3}O_x$	3	N115	80	1.69 V@1 A cm^{-2}	[33]
D-PtCu/CF	0.1	IrO_2	NA	NA	60	1.75 V@1 A cm^{-2}	[34]
MLG/Dend-Pt NPs	0.025	Ir black	2	N117	40	1.70 V@0.5 A cm^{-2}	[35]
$Pt_{0.25}$/Co	0.5	IrO_2	2	N117	50	1.69 V@1 A cm^{-2}	[36]
Pt,Ru,Rh,Pd,Re-$MoSe_2$	NA	IrO_2	NA	NA	80	1.82 V@1 A cm^{-2}	[37]
Pt_{SA}, P/np-MoS_2	NA	IrO_2	NA	N117	60	1.67 V@1 A cm^{-2}	[38]
Alloyed Pt SA	0.02	IrO_2	NA	N117	80	1.82 V@1 A cm^{-2}	[39]
Pt SLP	0.015	IrO_2	1	N115	90	1.71 V@1 A cm^{-2}	[40]
Ru-NPs/OPC-1.9 nm	0.05	IrO_2	1.5	N115	65	1.77 V@1 A cm^{-2}	[41]
Mo@Ru-3	4.5	IrO_2	2.5	N212	80	1.95 V@1 A cm^{-2}	[42]
Ru@NPCS	0.017	IrO_2	NA	NA	80	1.73 V@1 A cm^{-2}	[43]
Ru−Mo_2C/C	0.15	IrO_2	1.5	80μm	80	1.58 V@1 A cm^{-2}	[44]
RuSA@NiFe PPc	NA	IrO_2	NA	N117	80	2.27 V@2 A cm^{-2}	[30]
RuS_2@MoS_2	NA	NA	NA	NA	80	1.67 V@1 A cm^{-2}	[45]

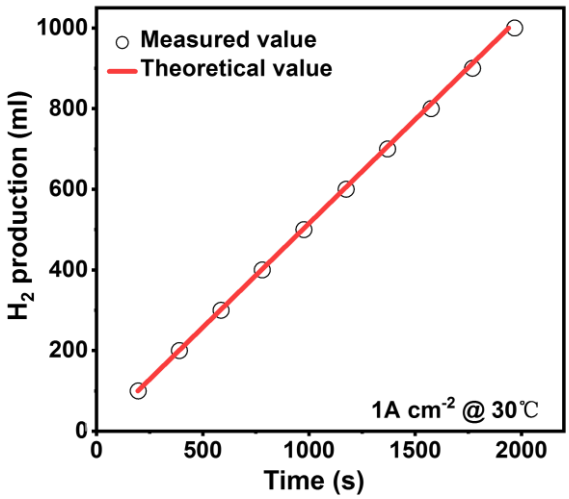

Supplementary Figure 38. The amount of H_2 theoretically calculated and experimentally measured in HEA-QDs/C cathode cell versus time at a current density of 1 A cm^{-2}.

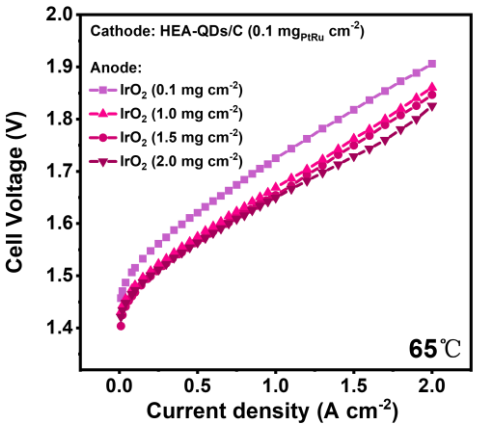

Supplementary Figure 39. Polarization curves of PEMWEs with various IrO_2 loadings.

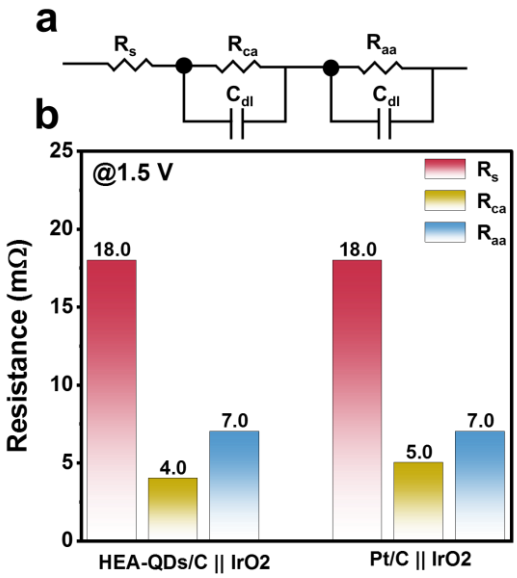

Supplementary Figure 40. (a) Typical equivalent electrical circuit model and (b) The resistance of R_s, R_{ca} and R_{aa} in PEMWE.

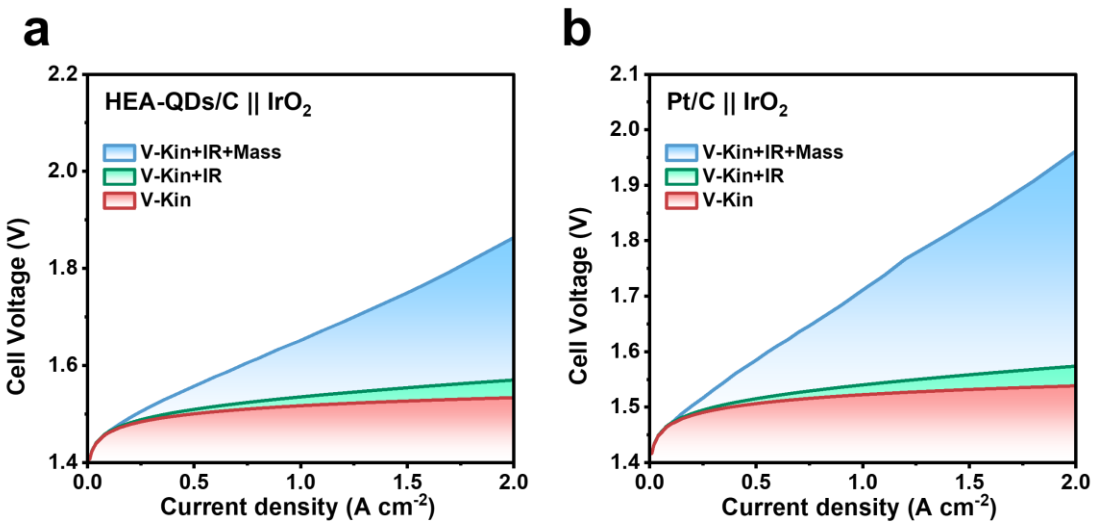

Supplementary Figure 41. The contribution of kinetic, ohmic and mass transport to the polarization curve of (a) the HEA-QDs/C cathode cell and (b) the Pt/C cathode cell.

References

1. T. Wu, J. Hong, Z. Lu, H. Wu, C. Wu, Z. Tang, X. Liu, B. Zeng, Y. Xu, G. Chen, C. Yuan and L. Dai, *Applied Catalysis B: Environmental*, 2021, **285**.
2. S. Rudi, C. Cui, L. Gan and P. Strasser, *Electrocatalysis*, 2014, **5**, 408-418.
3. J. Polonský, P. Mazúr, M. Paidar, E. Christensen and K. Bouzek, *International Journal of Hydrogen Energy*, 2014, **39**, 3072-3078.
4. G. Kresse and J. Furthmüller, *Physical review B*, 1996, **54**, 11169.
5. J. P. Perdew, K. Burke and M. Ernzerhof, *Physical review letters*, 1996, **77** 3865.
6. J. K. Nørskov, J. Rossmeisl, A. Logadottir, L. Lindqvist, J. R. Kitchin, T. Bligaard and H. Jonsson, *The Journal of Physical Chemistry B*, 2004, **108** 17886-17892.
7. K. Chan and J. K. Norskov, *J Phys Chem Lett*, 2015, **6**, 2663-2668.
8. S. Trasatti, *Pure and Applied Chemistry*, 1986, **58**, 955-966.
9. X. Yang, H. Ding, S. Li, S. Zheng, J. F. Li and F. Pan, *J Am Chem Soc*, 2024, **146**, 5532-5542.
10. L. Li, G. Zhang, B. Wang, T. Yang and S. Yang, *Journal of Materials Chemistry A*, 2020, **8**, 2090-2098.
11. F. Li, G. F. Han, H. J. Noh, I. Ahmad, I. Y. Jeon and J. B. Baek, *Advanced Materials*, 2018, **30**.
12. Q. Cheng, C. Hu, G. Wang, Z. Zou, H. Yang and L. Dai, *Journal of the American Chemical Society*, 2020, **142**, 5594-5601.
13. J. Mahmood, F. Li, S.-M. Jung, M. S. Okyay, I. Ahmad, S.-J. Kim, N. Park, H. Y. Jeong and J.-B. Baek, *Nature Nanotechnology*, 2017, **12**, 441-446.
14. J. Xu, M. Zhong, N. Song, C. Wang and X. Lu, *Chinese Chemical Letters*, 2023, **34**.
15. W. Zhao, C. Luo, Y. Lin, G.-B. Wang, H. M. Chen, P. Kuang and J. Yu, *ACS Catalysis*, 2022, **12**, 5540-5548.
16. B. Zheng, L. Ma, B. Li, D. Chen, X. Li, J. He, J. Xie, M. Robert and T.-C. Lau, *Catalysis Science & Technology*, 2020, **10**, 4405-4411.
17. Y. Chen, J. Li, N. Wang, Y. Zhou, J. Zheng and W. Chu, *Chemical Engineering Journal*, 2022, **448**.
18. N. Roy, K. T. Leung and D. Pradhan, *The Journal of Physical Chemistry C*, 2015, **119**, 19117-19125.
19. C.-B. Hong, X. Li, W.-B. Wei, X.-T. Wu and Q.-L. Zhu, *Applied Catalysis B: Environmental*, 2021, **294**.
20. Y. Liu, S. Liu, Y. Wang, Q. Zhang, L. Gu, S. Zhao, D. Xu, Y. Li, J. Bao and Z. Dai, *Journal of the American Chemical Society*, 2018, **140**, 2731-2734.
21. X. Ma, H. Xiao, Y. Gao, M. Zhao, L. Zhang, J. Zhang, J. Jia and H. Wu, *Journal of Materials Chemistry A*, 2023, **11**, 3524-3534.
22. W. Li, H. Zhang, K. Zhang, W. Hu, Z. Cheng, H. Chen, X. Feng, T. Peng and Z. Kou, *Applied Catalysis B: Environmental*, 2022, **306**.
23. M.-R. Gao, J.-X. Liang, Y.-R. Zheng, Y.-F. Xu, J. Jiang, Q. Gao, J. Li and S.-H. Yu, *Nature Communications*, 2015, **6**.

24. L. Fan, P. F. Liu, X. Yan, L. Gu, Z. Z. Yang, H. G. Yang, S. Qiu and X. Yao, *Nature Communications*, 2016, **7**.
25. Y. H. Li, P. F. Liu, L. F. Pan, H. F. Wang, Z. Z. Yang, L. R. Zheng, P. Hu, H. J. Zhao, L. Gu and H. G. Yang, *Nature Communications*, 2015, **6**.
26. T. T. Huynh, V. T. T. Mai, A. Q. K. Nguyen and H. Q. Pham, *Advanced Sustainable Systems*, 2024, **8**.
27. J. Wang, W. Zang, X. Liu, J. Sun, S. Xi, W. Liu, Z. Kou, L. Shen and J. Wang, *Small*, 2024, DOI: 10.1002/smll.202309427.
28. Y. Li, Z. Dou, Y. Pan, H. Zhao, L. Yao, Q. Wang, C. Zhang, Z. Yue, Z. Zou, Q. Cheng and H. Yang, *Nano Letters*, 2024, DOI: 10.1021/acs.nanolett.4c00495.
29. C. Xu, H. Yu, H. Huang, W. Huang, S. Li, Y. Cao, H. Lu, G. Li, Y. Li, X. Li, Y. Zhang and W. Chen, *Chemical Engineering Journal*, 2024, **489**.
30. Z. Kou, Y. Liu, W. Cui, B. Yang, Z. Li, R. D. Rodriguez, Q. Zhang, C.-L. Dong, X. Sang, L. Lei, T. Zhang and Y. Hou, *Energy & Environmental Science*, 2024, **17**, 1540-1548.
31. Z. Niu, Z. Lu, Z. Qiao, S. Wang, X. Cao, X. Chen, J. Yun, L. Zheng and D. Cao, *Advanced Materials*, 2024, **36**.
32. B. Jiang, H. Yuan, Q. Dang, T. Wang, T. Pang, Y. Cheng, K. Wu, X. Wu and M. Shao, *International Journal of Hydrogen Energy*, 2019, **44**, 31121-31128.
33. Z. Xie, S. Yu, G. Yang, K. Li, L. Ding, W. Wang, D. A. Cullen, H. M. Meyer, S. T. Retterer, Z. Wu, J. Sun, P.-X. Gao and F.-Y. Zhang, *Chemical Engineering Journal*, 2021, **410**.
34. M. Zhou, Y. Zhao, X. Zhao, P.-F. Yin, C.-K. Dong, H. Liu, X.-W. Du and J. Yang, *ACS Applied Energy Materials*, 2024, **7**, 3848-3857.
35. B. Devadas, M. Prokop, S. Duraisamy and K. Bouzek, *Electrochimica Acta*, 2023, **441**.
36. T. Wang, D. Zhang, J. Fei, W. Yu, J. Zhu, Y. Zhang, Y. Shi, M. Tian, J. Lai and L. Wang, *Applied Catalysis B: Environmental*, 2024, **343**.
37. z. luo, Y. Guo, C. He, Y. Guan, L. Zhang, Y. Li, Q. Zhang, C. He, X. Sun and X. Ren, *Angewandte Chemie International Edition*, 2024, DOI: 10.1002/anie.202405017.
38. J. Peng, Z. Wang, K. Jiang, M. Peng, N. Palaniyandy, J. Ren and Y. Tan, *Journal of Materials Chemistry A*, 2024, DOI: 10.1039/d4ta01738b.
39. H. Gao, Y. Jiang, R. Chen, C. L. Dong, Y. C. Huang, M. Ma, Z. Shi, J. Liu, Z. Zhang, M. Qiu, T. Wu, J. Wang, Y. Jiang, J. Chen, X. An, Y. He and S. Wang, *Advanced Functional Materials*, 2023, **33**.
40. J. Song, Y. Kim, J. Lee, H.-J. Kim, Y.-E. Sung, T. Lim and O. J. Kwon, *ACS Sustainable Chemistry & Engineering*, 2023, **11**, 16258-16266.
41. H. Zhao, J. Li, J. Zou, Y. Tan, C. Chen, B. Yang, Q. Cheng and H. Yang, *Journal of Materials Chemistry A*, 2023, **11**, 18262-18271.
42. Z. Zhang, P. Li, Q. Wang, Q. Feng, Y. Tao, J. Xu, C. Jiang, X. Lu, J. Fan, M. Gu, H. Li and H. Wang, *Journal of Materials Chemistry A*, 2019, **7**, 2780-2786.
43. R. Ma, X. Wang, X. Yang, Y. Li, C. Liu, J. Ge and W. Xing, *Nano Research*, 2022, **16**, 166-173.
44. Y. Li, Z. Dou, Y. Pan, H. Zhao, L. Yao, Q. Wang, C. Zhang, Z. Yue, Z. Zou, Q. Cheng

and H. Yang, *Nano Letters*, 2024, **24**, 5705-5713.
45. M. Sarno and E. Ponticorvo, *International Journal of Hydrogen Energy*, 2019, **44**, 4398-4405.